# High-resolution 3-D imaging of electron density perturbations using ultra-dense GNSS observation networks in Japan: an example of medium-scale traveling ionospheric disturbances

Weizheng Fu[1]*, Yuichi Otsuka[1] and Nicholas Ssessanga[2]

**Abstract**

For the first time using computerized ionospheric tomography (CIT) and leveraging ultra-dense slant total electron content (STEC) measurements derived from two ground-based Global Navigation Satellite System (GNSS) receiver networks in Japan, we have reconstructed the 3-D field-aligned structure of nighttime medium-scale traveling ionospheric disturbances (MSTIDs) with high spatiotemporal resolution. The CIT algorithm focuses on electron density perturbation components, allowing for the imaging of disturbances with small amplitudes and scales. Slant TECs used for CIT are setup to consist of two components: the background derived from IRI-2016 model and TEC perturbations obtained by subtracting a 30-min running average from observations. The resolution is set to 0.25º in latitude and longitude, 10 km in altitude, 30 s in time. Simulations were conducted to assess the performance of the CIT algorithm, revealing that this technique has good fidelity by accurately reconstructing more than 80% of the electron density perturbations. The focus is on the nighttime event of July 4, 2022, when data were accessible. The reconstruction results show that the MSTIDs initially form at lower altitudes and subsequently develop to exhibit large amplitudes and scales that extend to higher altitudes, characterized by a well-defined frontal structure with electrodynamic signatures. These results are consistent with theories and snippets of observational evidence regarding electromagnetic-influenced MSTIDs, hence affirming the effectiveness of the developed CIT technique in probing of the variations in the 3-D structure of ionospheric electron density. This is expected to contribute to a compressive understanding of the underlying mechanisms of ionospheric inhomogeneities.

**Keywords** GNSS-TEC, 3-D tomography, Electron density perturbation, Nighttime MSTIDs
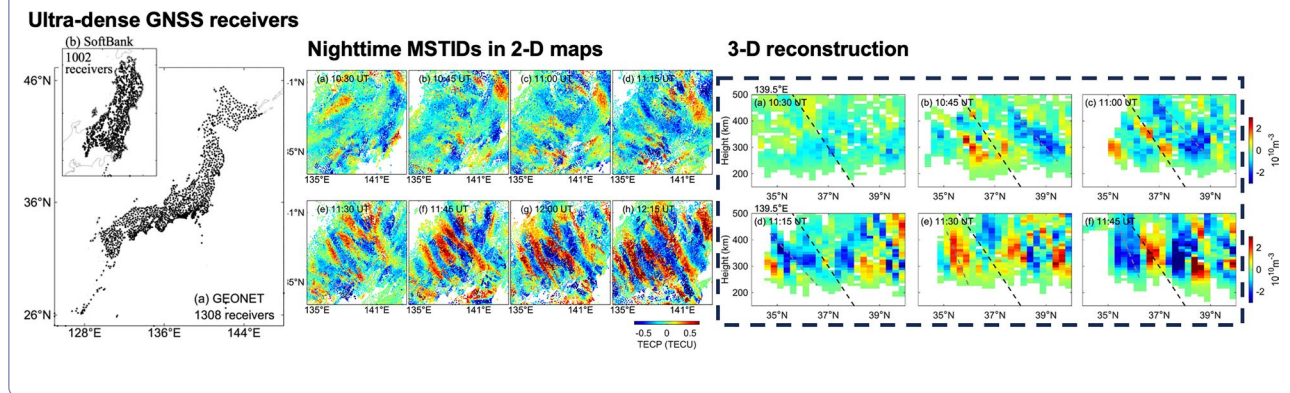
*Correspondence:
Weizheng Fu
fu.weizheng@isee.nagoya-u.ac.jp
Full list of author information is available at the end of the article

Fu *et al. Earth, Planets and Space*　　(2024) 76:102

Page 2 of 13

**Graphical Abstract**



## 1 Introduction

The ionosphere is a dynamic and complex geospace region, primarily influenced by solar radiation, geomagnetic disturbances, and activities in the lower atmosphere. Disturbances in the ionosphere can interfere with radio signal propagation, potentially reducing the reliability of systems reliant on trans-ionospheric signals, such as satellite navigation, communication, and timing services. Therefore, achieving accurate imaging and characterization of ionospheric disturbances is pivotal in understanding the underlying mechanisms of ionospheric irregularities, which significantly influence error corrections in various applications.

Ionospheric disturbances cover a vast range of phenomena, resulting from the complex permutations of a broad spectrum of intricate ionospheric drivers, which dynamically change with time. In this study, we only focus on the nighttime medium-scale traveling ionospheric disturbances (MSTIDs), a common type of ionospheric perturbations at mid-latitudes, particularly during the summer period. These disturbances are characterized by wavelike plasma density perturbations in the ionospheric F region, exhibiting horizontal wavelengths spanning a few hundred kilometers and periods of several tens of minutes (Hunsucker 1982). Despite extensive study using various techniques such as ionosondes (Bowman 1990), radars (Behnke 1979), and airglow images (Shiokawa et al. 2003a), a comprehensive understanding of the physical mechanisms behind the generation and development of MSTIDs remains elusive. One contributing factor is the limited observation coverage or spatiotemporal resolution inherent in many observational techniques, which prevents complete imaging of the morphologies and dynamics of MSTID structures.

In recent years, the development of Global Navigation Satellite System (GNSS) techniques has significantly mitigated this challenge, emerging as a highly effective tool for ionospheric study (Jin et al. 2022). The principal parameter derived from GNSS observables is the integrated electron density, known as slant total electron content (STEC), measured along the line of sight (LOS) between the transmitter (on-board the satellite) and receiver (ground station); STEC correlates with signal group delay or phase advance. Indeed, the rapid advancements in GNSS infrastructure, particularly receivers, have enabled effective monitoring and analysis of the ionosphere. In Japan, the GNSS Earth Observation Network System (GEONET) is an ideal resource for MSTID studies (e.g., Saito et al. 1998; Otsuka et al. 2011; Fu et al. 2022), due to its nationwide coverage of over 1300 stations with an average spacing of 20–25 km and a temporal resolution of 30 s. In addition, another GNSS observation network in Japan provided by SoftBank Corp. (referred to as "SoftBank" hereafter), is currently available. This network includes more than 3,200 stations, about 2.5 times the number of GEONET receivers. Fu et al. (2024) demonstrated the effectiveness of combining these two dense networks for studying MSTIDs in detail. While these results are promising, the integrated nature of STEC and limitations in GNSS-Earth geometry constrain direct or simplistic analyses. For instance, utilizing a single-thin-shell model (Mannucci et al. 1998) only offers insight into the two-dimensional (2-D) horizontal structure of ionospheric dynamics. The absence of the height dimension poses a substantial limitation on the depth of information we can infer. The utilization of ultra-dense GNSS observations over Japan currently available can potentially enable the reconstruction of a continuous and broad three-dimensional (3-D) distribution of ionospheric electron density (IED) perturbations with a high spatiotemporal resolution, thereby

enhancing our understanding of the ionospheric disturbances such as MSTIDs.

Computerized ionospheric tomography (CIT), first proposed by Austen et al. (1988), has been used to reconstruct IED distributions in a vertical plane using a large number of irregularly sampled GNSS-TEC measurements. The effectiveness of CIT in 3-D ionospheric reconstruction has been confirmed in many studies, e.g. Lu et al. (2021) and references therein. Recently, tomography methods have successfully been employed to reconstruct the 3-D structures of MSTIDs (Ssessanga et al. 2015; Chen et al. 2016; Song et al. 2021). However, due to the limited spatial resolution ((1°–2°) in latitude and longitude, 10–30 km in altitude) caused by the insufficient number of signal rays, capturing the 3-D dynamics and morphology of MSTID structures with electrodynamic signatures during their evolution has remained a crucial yet challenging task. In this research, we develop a 3-D tomography technique to reconstruct electron density perturbations based on ultra-high-density GNSS observations over Japan. Our reconstructions provide the first high-resolution tomography evidence that the vertical structures of nighttime MSTIDs align along the geomagnetic field lines. The data used in this analysis and a concise mathematical description of the tomography approach are introduced in Section "Data and algorithm". Section "Simulation" presents the validity and evaluates the performance of this tomography technique through simulation. Section "Reconstruction results of nighttime MSTIDs" shows the reconstruction results for an MSTID event using real observations. Finally, Section "Conclusions" concludes the paper.

## 2 Data and algorithm

Complementary to the overview of GEONET and SoftBank in the introduction, the latter network was established in late 2019 by the Japanese telecommunications giant, Soft-Bank, with the primary aim of offering the public high-precision positioning services for a variety of applications. The black dots in Fig. 1 represent the distribution of GNSS receivers used in this research, provided by GEONET and SoftBank. To be noted, due to data access limitations and the occurrence rate of nighttime MSTIDs (Shiokawa et al. 2003a), we have only a portion of the SoftBank data (1,002 receivers; concentrated in the northeast part of Honshu Island) for one event of nighttime MSTIDs on July 4, 2022. During this event, the available number of receivers from GEONET and SoftBank is 2,310. Multi-GNSS data with a data cadence of 30 s from GEONET (including GPS, GLONASS, and Galileo) and SoftBank (including GPS, GLONASS, and BeiDou) were integrated to generate ultra-dense observations over Japan. A cutoff elevation angle of 30° is set to avoid multipath effects (Tsugawa et al. 2007).
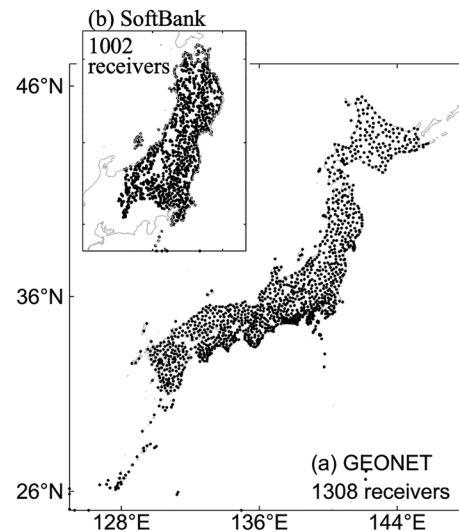


**Fig. 1** Distribution of GNSS stations provided by **a** GEONET and **b** SoftBank Corp. used in this research

Following Fu et al. (2022), to identify and characterize the perturbations caused by nighttime MSTIDs effectively, total electron content perturbations (TECPs) were computed by subtracting a 30-min running average (centered on the LOS epoch) from each STEC value. Arc segments that were less than 30 min were not used to avoid any spurious perturbations. Theoretically, utilizing TECP rather than absolute TEC avoids the effects of instrumental biases and clock errors from different GNSS constellations, allowing for a more consistent and accurate estimation of ionospheric perturbations.

The primary focus for our tomography analysis is the F region, which is the most electron-dense area in the ionosphere. The intersection of GNSS signals with various ionosphere altitudes enables a 3-D representation of IED through CIT. In this research, the CIT approach follows the voxel-based model. The 3-D region volume under examination is divided into $n$ voxels. Each voxel ($j$) is assumed to have an unknown uniform distribution of electron densities ($x_j$). Subsequently, the LOS STEC ($y_i$) is formulated as a finite summation over these voxels

$$y_i = \sum_{j=1}^{n} a_{ij}x_j + e_i, \tag{1}$$

where $a_{ij}$ denotes the length of the signal ray traversing through intersected voxel ($j$); this value is zero if the ray does not intersect with the voxel. The term $e_i$ represents both instrumental and representative errors. For many STEC measurements, Eq. 1 can be expressed in a compact matrix form as

$$\vec{Y} = A\vec{X} + \vec{E}. \qquad (2)$$

In fact, the limited geometry of satellite-ground receiver configurations and restrictions on exposure time to avoid averaging dynamics, result in the number of measurements (*m*) being generally far less than the necessary number of unknowns (*n*). To solve the ill-posed and ill-conditioned inverse problem in Eq. 2, we employed the multiplicative algebraic reconstruction technique (MART) following Ssessanga et al. (2015) and Fu et al. (2021), because it is memory efficient and ensures positivity

$$x_j^{k+1} = x_j^k \left( \frac{y_i}{< \vec{a}_i, \vec{X}^k >} \right)^{\lambda_k a_{ij}/\|a_{ij}\|}, j = 1,2,3,\dots,N, \quad (3)$$

where $\vec{a}_i$ represents the *i* th row vector in matrix $A$; $x_j^k$ is the *j* th unknown at the *k* th iteration; $< \vec{a}_i, \vec{X}^k >$ is the simulated TEC, calculated as the inner product of the *i* th row of $A$ and a column vector of $\vec{X}$ values at the *k* th iteration; and $\lambda_k$ is the relaxation factor, which is chosen within the range $0 < \lambda_k < 1$ and is set to 0.2 in this work. The convergence of MART was determined when absolute change between iterations, expressed as $\left([X^{k+1} - X^k]/X^k\right) \times 100 < e$, where $e$ is the stopping criterion, in this case 0.05%.

The computational procedure of MART in Eq. 3 requires an initial guess $(\vec{X}_0)$, which impacts both the fidelity and the rate of convergence. In this research, we generate the background electron density $(\vec{X}_0)$ using the International Reference Ionosphere (IRI)-2016 model (Bilitza et al. 2017). This can help produce a smooth $\vec{X}_0$ for the iterative method and establish a consistent baseline for the analysis. User-entered parameters include time, latitude, and longitude; other parameters remain at default inputs. For the calculation process, time input to the IRI model varies according to the time of the TEC observations. Considering our focus is more on the TEC perturbation components caused by ionospheric disturbances rather than absolute TEC values, the LOS STEC from each observation used in tomography ($STEC_{tomo}$) can be computed as the sum of two components: the integration of background electron density (generated by IRI model) along the actual geometry of signal rays ($STEC_{bcg}$), and the TEC perturbations components at the calculation epoch

$$STEC_{tomo} = STEC_{bcg} + TECP. \qquad (4)$$

With these STEC measurements, a 3-D representation of IED perturbations can be readily achieved. Moreover, this process enables faster convergence and offers the potential to image perturbations with smaller amplitudes and scales due to the low noise and minimal discrepancy between the background and observation data.

## 3 Simulation

According to the distribution of ground-based GNSS receivers, the 3-D region analyzed in this study on July 4, 2022 spans a spatial volume from 32° N to 40° N in latitude, and from 133° E to 142° E in longitude, covering altitudes ranging from 100 to 800 km. With a resolution of 10 km in altitude and 0.25° in both latitude and longitude, the total number of unknowns was 80,640. The time resolution was set to 30 s. This size of the inverse problems is manageable on a Laptop with 16 gigabytes of memory, and the iterative procedure completes within 10 min.

Before conducting reconstructions with observational data, we perform a simulation to evaluate the performance in reproducing a consistent representation of the ionospheric perturbations in the F region. Figure 2a shows the spatial distribution of the slant TEC ray paths at 09:30 UT (universal time) on July 4, 2022, in the 3-D domain. Despite presenting only one-twentieth of the total paths (due to image visibility), the dense distribution of signal rays penetrating the ionosphere is evident, especially in the vicinity of the SoftBank network. To indicate the spatial distribution of this dense dataset, subplot (b) shows the distribution of signal ray path azimuths at that epoch. It can be observed that the inclusion of multi-GNSS observations (GLONASS, Galileo, and BeiDou) improves the spatial distribution of ray paths compared to including only GPS data, particularly in the southwest (~180°–270°) and north-northwest (~315°–360°) directions. These enhancements in ray path density and spatial distribution, which provide rich information on the ionosphere, may facilitate the reconstruction of high-resolution 3-D imaging of the electron density perturbations.

Following Fu et al. (2024), the solvability performance within the analyzed region is quantified by calculating the percentage of voxels classified as solvable. This is expressed as $N_1/N_0$, where $N_0$ represents the total number of voxels in the analyzed region, and $N_1$ is the number of voxels with signal ray penetration. In the calculation, ray paths intersecting the minimum boundary region were excluded, since it is challenging to ascertain the densities traversed by the portion of the ray beyond the boundary. For this event, about 8,000 ray paths from multi-GNSS observations (GPS, GLONASS, Galileo, and BeiDou) penetrate the tomography region. Figure 2c shows the time variation of solvability during 09:00–10:00 UT. Within this period, about 55% of the voxels are solvable. That is to say, despite the high spatiotemporal
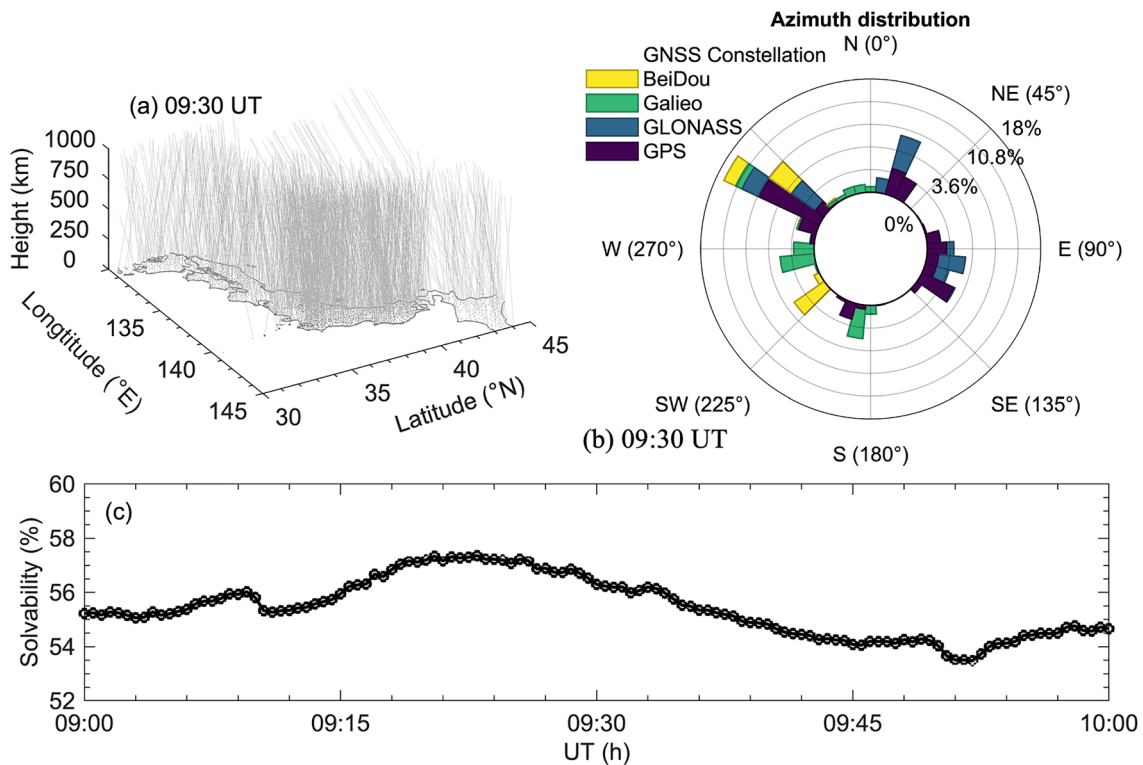
**Fig. 2** Distribution of slant TEC paths of **a** ground-based receivers and **b** ray path azimuths at 09:30 UT, on July 4, 2022. **c** Time variation of solvability during 09:00–10:00 UT

resolution, the 3-D reconstruction benefits from a relatively large number of observations that provide ample information in the tomography region.

In the simulation case, disturbances were added along the NE-SW line from (39.5° N, 141.5° E) to (35.5° N, 137.5° E) within the region that has the most data points over Japan. Figure 3a shows the background electron density at 09:30 UT, July 4, 2022, generated by the IRI-2016 model along the NE-SW line. Subplot (b) presents the 2-D maps of input disturbances at 300-km altitude. In the vertical dimension, to simulate the undulation relation of height and electron density perturbations (e.g., Ssessanga et al. (2017) and reference therein), wavelike enhancements or depletions were input in this region. As shown in subplot (d), these disturbances have variations in electron density with respect to altitude in each longitudinal and latitudinal grid, with the fluctuations occurring between altitudes of 100–500 km. In subplots (b) and (d), the voxels outside the simulated disturbances represent the background without perturbations. The white curves represent the height of the local maximum or minimum simulated perturbations in each longitudinal and latitudinal grid, and the black lines indicate the simulated TEC perturbation values. The amplitudes of the input vertical disturbances at each specified position are about ±0.5

TECU (TEC unit; 1 TECU $=10^{16} el/m^2$), which is a typical value observed during nighttime MSTID event, and is about 3% of the background TEC. Such small input amplitudes and wavelike structures can be a good indicator of the reconstruction performance under complex background conditions. In such a case, the simulated ionosphere can be computed as the sum of this background (subplot (a)) and the perturbed ionosphere (subplots (b) and (d)). Based on this simulated ionosphere, the simulated STEC data for tomography were then generated as an integral of electron density along the ray paths determined from the real geometry of GNSS satellites and receivers at 09:30 UT, July 4, 2022.

Figure 3c and e show the reconstructed structures in the horizontal (at 300-km altitude) and vertical planes, respectively, after subtracting the background ionosphere shown in subplot (a). It is evident that this CIT technique enables the successful reconstruction of electron density perturbations with small amplitudes and scales. From subplot (c), at an altitude of 300 km, it is observed that the positive/negative disturbances can be reconstructed at positions corresponding to those in the input. The observed reduction in amplitude (about 30%) may be associated with the blurring of reconstructed structures in both horizontal and vertical dimensions. These errors
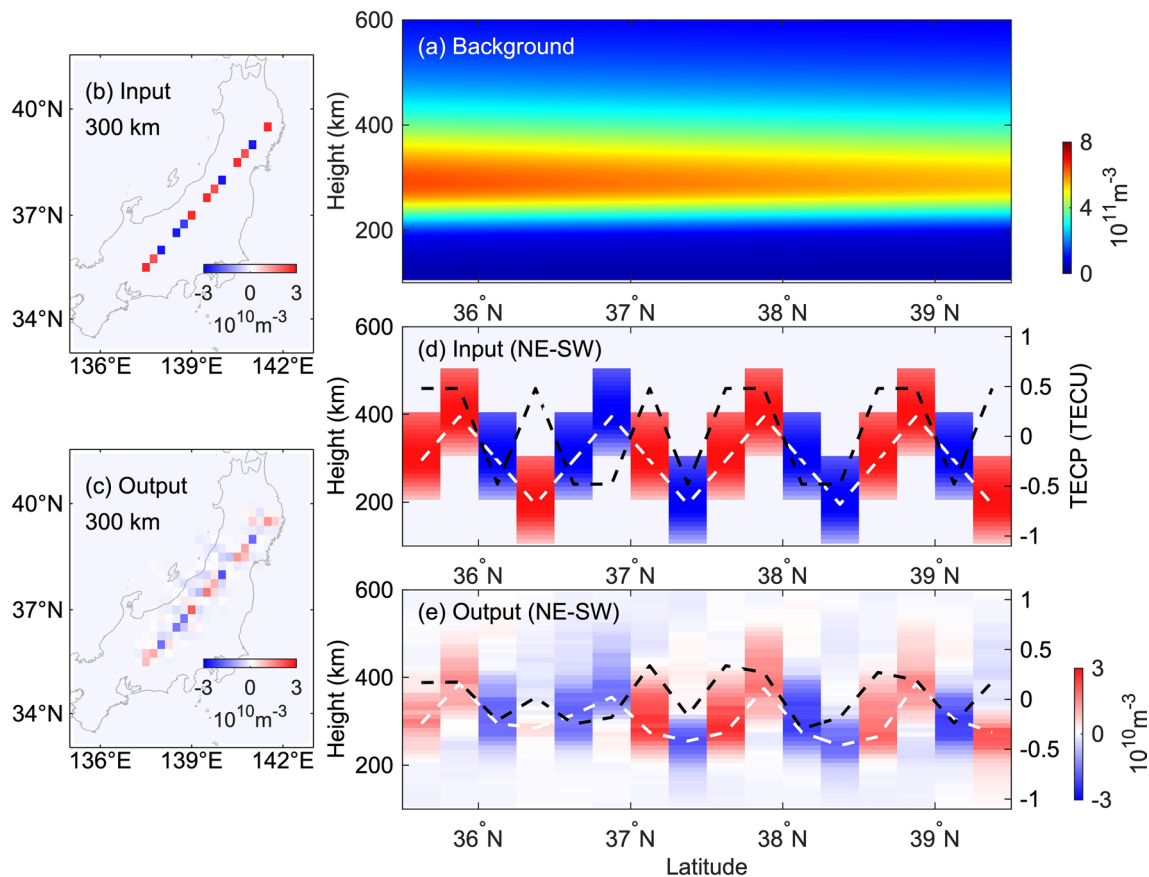
Fu *et al. Earth, Planets and Space* (2024) 76:102

Page 6 of 13

**Fig. 3 a** Background ionosphere generated by the IRI-2016 model at 09:30 UT, July 4, 2022. 2-D maps of **b** input and **c** output disturbances at 300 km. Vertical structure of **d** input and **e** output disturbances along the northeast-southwest plane. In subplots (**d**) and (**e**), the white curves represent the height of the local maximum or minimum simulated perturbations in each longitudinal and latitudinal grid corresponding to the left y-axis, and the black lines indicate the simulated TEC perturbation values corresponding to the y-axis on the right side. Subplots (**d**) and (**e**) have the same color scale

potentially stem from representational errors inherent in the tomography process, as well as from the limited slant signal ray paths penetrating all the simulated disturbances with small scales. In the vertical plane, as shown in subplot (e), the wavelike fluctuations can also be reconstructed, albeit with some underperformance in amplitude. A correlation of 86.63% is observed between the local maximum/minimum heights of disturbances as simulated and reconstructed. This high correlation suggests that this tomography technique has sufficient sensitivity to quantitatively capture the vertical variations observed during the MSTID event. Additionally, it is observed that the majority of densities are reconstructed within the altitude range of 200–500 km. One possible cause is that the coverage of ionospheric pierce points (IPPs) at lower altitudes (< 200 km) is naturally smaller than at higher altitudes, thus providing limited information. Another factor could be the limitations of the MART algorithm as identified in Kunitsyn and Tereshchenko ([2003]); when features were situated in regions of low electron density, MART had a propensity to reconstruct these features towards areas of higher electron density, particularly around the hmF2 point. Fortunately, as nighttime MSTIDs mainly exhibit vertical fluctuations within the altitude range of 200–500 km (Yang et al. [2015]), this limitation is unlikely to significantly affect our analysis. Furthermore, at lower latitudes, a particular underperformance in terms of reconstructed amplitude and local maximum/minimum height is observed (< 37° N). This phenomenon could be attributed to the relatively sparse distribution of GNSS observations in the region outside the SoftBank observation network. Similar underperformance of 2-D reconstruction near the boundary of the SoftBank network has also been observed in Fu et al. ([2024]).

As mentioned earlier, the initial guess ($\vec{X}_0$) plays a crucial role in the iterative process and may contribute to the poor reconstruction at lower altitudes (< 200 km). In theory, the background ionosphere generated by the IRI model may not perfectly match the actual ionosphere. To analyze the effects of different initial guess and further validate the effectiveness of this method, we use different $\vec{X}_0$ by adjusting the hmF2 (the height of the peak electron density) to be 100 km lower or higher than the original value, as shown in Fig. 4a and d. The input disturbances are the same as those depicted in Fig. 3b and d. Figure 4b, c and e, f show the reconstructed structures in the vertical and horizontal (at 300-km altitude) planes for different hmF2 cases. Based on these reconstruction results, the wavelike perturbations can still be reconstructed in both the horizontal and vertical planes, but with a degraded performance. To quantify this underperformance, Fig. 5 shows the distribution of reconstruction

errors in the different cases. Results from all data points were used in the calculations to provide a comprehensive perspective. It can be observed that, when hmF2 is decreased (increased) 100 km, the standard deviation ($\sigma$) increases from 0.0157 to 0.0268 (0.0363) TECU. The percentage of the data falling within $\mu \pm \sigma$ decreases from 86.34% to 84.75% (85.69%). In such scenarios, although the background affects the reconstruction performance to a certain extent, the tomography technique can still reconstruct the 3-D structures of electron density perturbations. However, when a background that does not match with the perturbations is used, the most obvious underperformance occurs in the altitude ranges where the background electron density concentration is small. For example, in Fig. 4(e), the perturbations at altitudes less than 300 km are not well reconstructed (with reduced amplitudes).
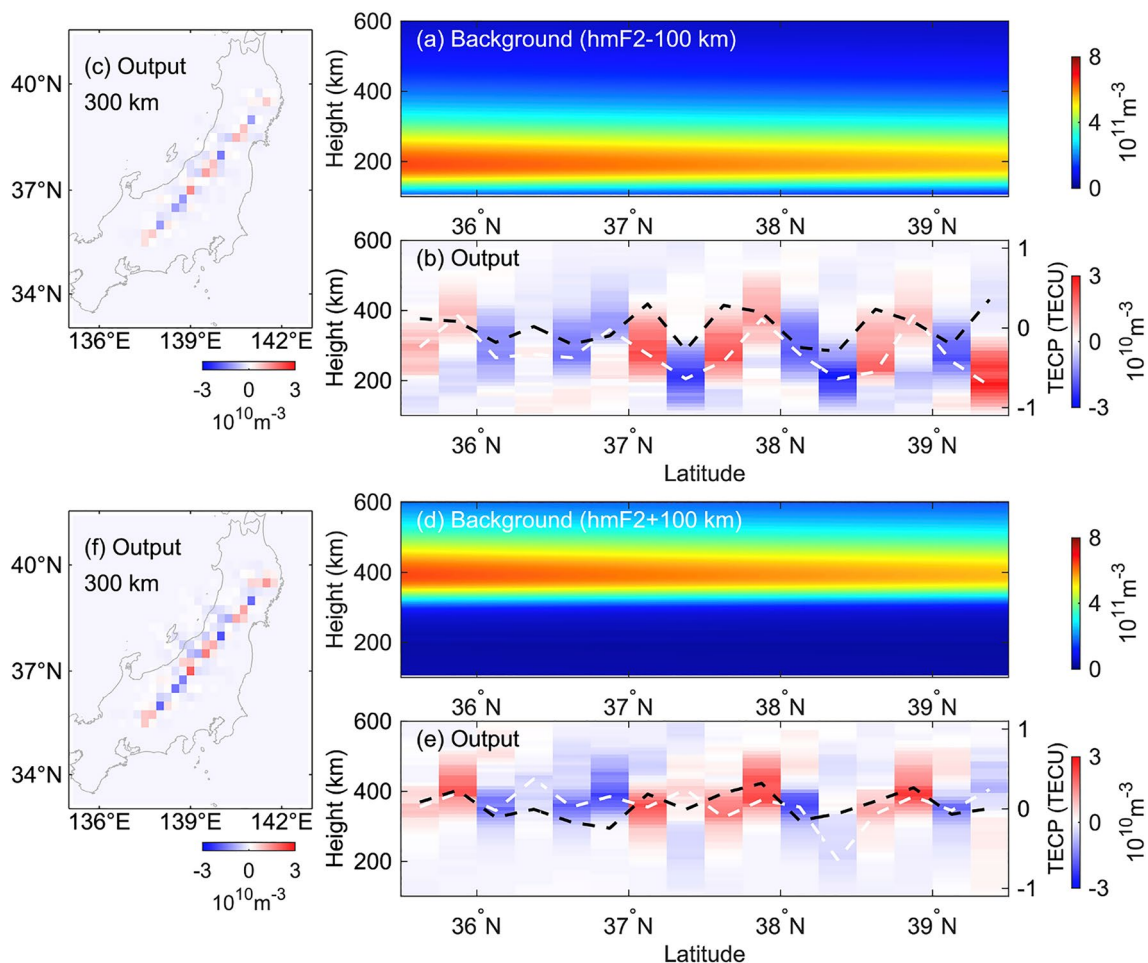


**Fig. 4** Simulation cases use different backgrounds for initial guesses. The input disturbances remain the same as those shown in Fig. 3
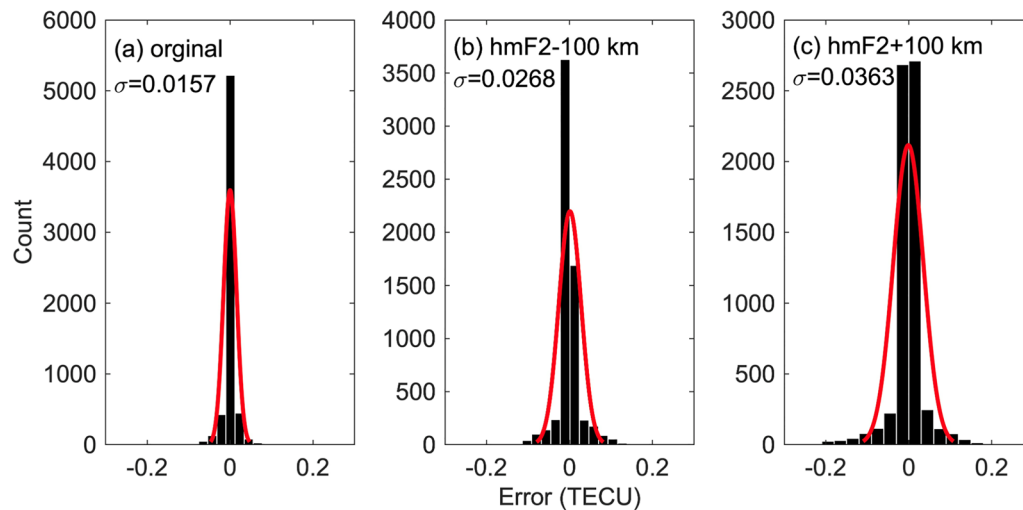
Fu *et al. Earth, Planets and Space*     (2024) 76:102

Page 8 of 13



**Fig. 5** Distribution of reconstruction errors for the different scenarios with accurately or inaccurately defined hmF2

## 4 Reconstruction results of nighttime MSTIDs

In this study, we use the nighttime MSTID event on July 4, 2022, as a representative case for further validation and analysis. This event occurred under geomagnetic quiet conditions ($|Dst| < 30$). For summer nighttime MSTID cases, sporadic E (Es) layers in the E region usually occur simultaneously and are electrodynamically coupled with MSTIDs (Cosgrove and Tsunoda 2004; Yokoyama et al. 2009; Fu et al. 2023). Es layers are mainly influenced by tidal effects, predominantly fluctuating around the 100-km altitude (Haldoupis 2012). As demonstrated in the previous simulation section, small perturbations at lower altitudes ($< 200$ km) cannot not be well reconstructed by the tomography technique. Therefore, during the reconstruction process, the additional contribution from lower altitudes ($< 200$ km) may be smeared into the F-region altitudes, hence leading to higher CIT amplitudes. However, due to their thin thickness ($\sim 1$ km, see Yamamoto et al. (1998)), the amplitudes of Es are generally smaller compared to MSTIDs and thus do not significantly affect the reconstruction amplitude in the F region. In this research, we assume that the electron density perturbations along the signal ray paths primarily originate from the F region.

Figure 6(a–h) shows the snapshots of 2-D TECP maps at different time epochs from 10:30 to 12:15 UT (19:30–21:15 JST (Japan Standard Time)) on 4 July 2022. These maps depicting nighttime MSTIDs, with a time resolution of 15 min, are obtained by using the single-layer model (SLM) mapped to an altitude of 300 km following Tsugawa et al. (2018). After about 10:45 UT, the appearance of northwest-southeast (NW–SE) aligned frontal structures with a southwestward propagation at around 36° N–37° N suggests the onset of nighttime MSTIDs.

Despite the small initial amplitudes and scales, these NW–SE structures have large growth rates, exhibiting substantial increases in amplitude and scale by 11:30 UT. Subsequently, MSTIDs are prevalent over Japan and develop to reach their maximum amplitude and scale within the region of interest. From the horizontal perspective, the rapid development of the NW–SE structures is clearly observed. This prompts the questions: how are structures defined in the vertical plane, and how do they manifest? The 3-D tomography analysis provides an insight by unveiling the vertical structure of electron density perturbations.

Before conducting the analysis, it is necessary to validate this tomography technique using real observations. Figure 6(i–l) are the 2-D TECP maps obtained by vertically integrating electron density perturbations from the tomography reconstructions. At 11:00 and 11:30 UT, when the amplitude is low and the perturbation less structured, SLM and CIT show an obvious lack of correlation. We anticipate that in such a case, the amplitudes could fall within the noise range, causing the smearing effect of MART to average the voxel density to a uniform and smooth value, as observed in the simulation section. In addition, another explanation could be related to the MSTID alignment in the vertical plane, where the structures are not vertically tilted. At the same position, the integration of positive and negative disturbances at different heights leads to small total perturbation values. Further details will be discussed later. At 12:00 and 12:15 UT, the perturbation components are well developed and structured. A relatively good correlation between frontal structures from SLM and CIT can be observed. Note that due to the spatial distribution of receivers, the region of higher reconstruction fidelity is located near the Japanese
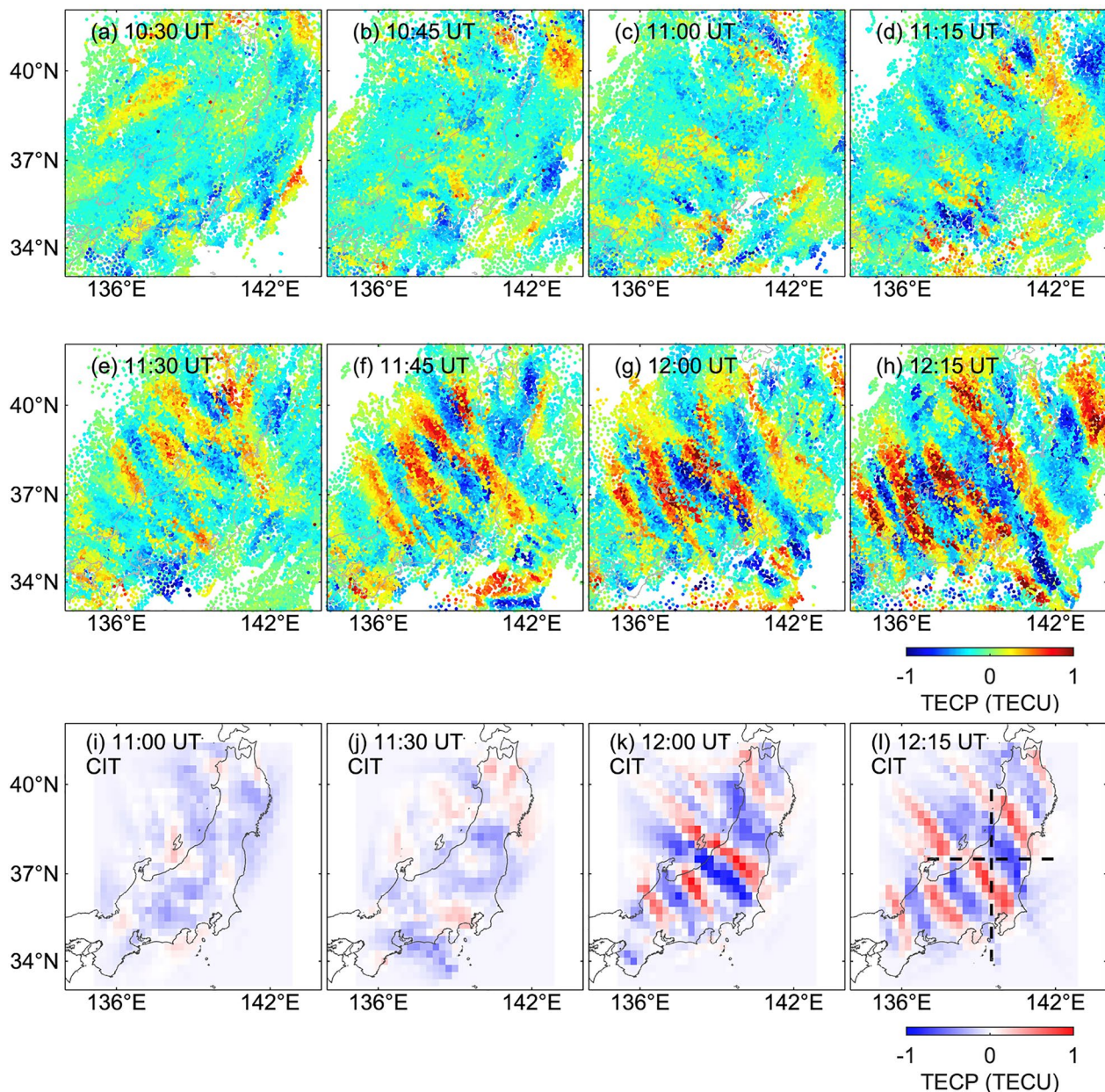
Fu *et al. Earth, Planets and Space*     (2024) 76:102

Page 9 of 13



**Fig. 6** Snapshots of 2-D TECP maps at different time epochs from 10:30 to 12:15 UT on July 4, 2022, obtained by using (**a–h**) single-layer model (SLM) at 300-km altitude and (**i–l**) tomography. The black dashed lines in subplot (l) indicate two vertical planes slicing in the zonal (37° N) and meridional (139.5° E) cross sections

landmass. Consequently, we have selected two vertical planes slicing through this region for further analysis; these planes are indicated by black dashed lines in subplot (l) and correspond to the zonal (37° N) and meridional (139.5° E) cross sections.

Figure 7 shows the vertical structures of reconstructed electron density perturbations in the meridional cross section at 139.5° E at different time epochs from 10:30 to 11:45 UT on July 4, 2022. The black dashed lines

indicate the geomagnetic field line at (39° N, 139.5° E) calculated from the International Geomagnetic Reference Field (IGRF)–13 model (Alken et al. 2021). The gray dashed lines represent the alignment of the apparent frontal structures in the vertical plane. Voxels where electron density perturbations remain unchanged after the tomography calculation are not plotted. In Fig. 7, electron density perturbations with small amplitude (~ 2–3% of the background maximum density) and scales
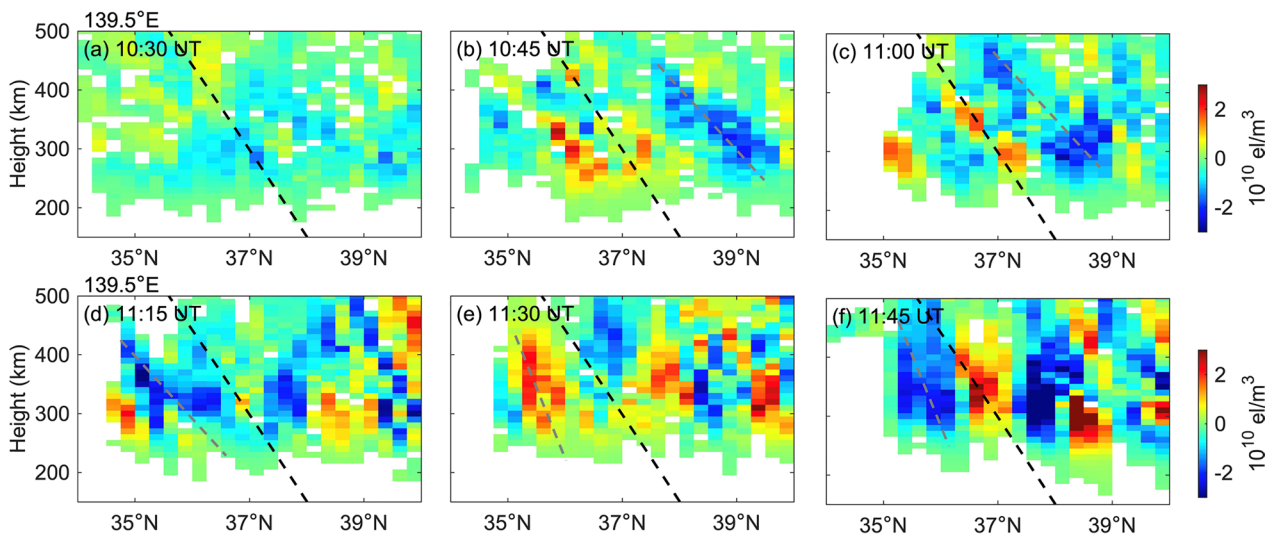
**Fig. 7** Vertical structures of reconstructed electron density perturbations at 139.5° E at different time epochs from 10:30 to 11:45 UT on July 4, 2022. The black and gray dashed lines indicate the geomagnetic field line and the alignment of the apparent frontal structures in the vertical plane, respectively

(~ 100 km) at 36° N–37° N are reconstructed in the vertical domain after 10:45 UT, consistent with the 2-D maps shown in Fig. 6.

Clearly, the 3-D reconstruction results provide information that cannot be obtained from the 2-D observations. In Fig. 7, the formation of MSTID structures initially occurs at lower altitudes (about 250–350 km) where the electron density gradient is steep. Subsequently, with increasing in amplitude and scale, MSTIDs develop and extend to higher altitudes (about 300–500 km). Particularly, these bands are not tilted vertically. An obvious tilt parallel to the geomagnetic field lines is observed in the meridional cross section, running from the high-south (lower latitudes) to the low-north (higher latitudes) direction. This feature is consistent with previous observations carried out by Seker et al. (2008), who have inferred an equatorward tilt with altitude of nighttime MSTIDs using vertical profiles of electron density measured by the Arecibo incoherent scattering radar, along with the observed southward shift of electron density perturbations. Now, with the developed CIT technique, we can directly derive this conclusion from the 3-D structures of electron density perturbations. Complementary, Shiokawa et al. (2003b) demonstrated a similar vertical alignment parallel to the geomagnetic field lines in meridional and vertical cross sections through model calculations of electron density perturbations caused by an oscillating electric field. Such a field-aligned alignment of electron density perturbations indicates the electrodynamic signatures of nighttime MSTID structures. Polarization electric fields, which are transmitted along the geomagnetic field lines, could play an important role in generating electron density perturbations. The electron density on the bottom side of the F layer decreases (increases) in regions where the F layer is lifted to higher altitudes (pushed down to lower altitudes). Perkins instability is the most likely mechanism accounting for the NW–SE structure (Perkins 1973). It suggests that plasma on a specific magnetic flux tube is lifted or pushed down by polarization electric fields, leading to the growth of the perturbation under certain conditions. The observed development of electron density perturbations aligns with the predictions of Perkins instability.

Notably, at 11:45 UT, the MSTID bands become more vertically aligned. One possible explanation for this phenomenon could be the nonlinear effects of instability and/or secondary instability in the MSTID structures, such as gradient drift instability (e.g., Kelley and Fukao, (1991)), when the amplitude of electron density perturbations becomes large. Another potential contributor could also be related to the TEC perturbations obtained from TEC measurements for each satellite-receiver pair; that is to say, for the case of MSTIDs exhibiting a phasefront elongating along the NW–SE direction, the TEC perturbations for satellites moving from northwest to southeast are smaller compared to those for satellites moving from southwest to northeast. This discrepancy may become more pronounced when MSTIDs of large amplitude and scale prevail over Japan, potentially leading to reconstruction errors. Further analysis is needed to determine the factors influencing the observed changes in the tilt angle.
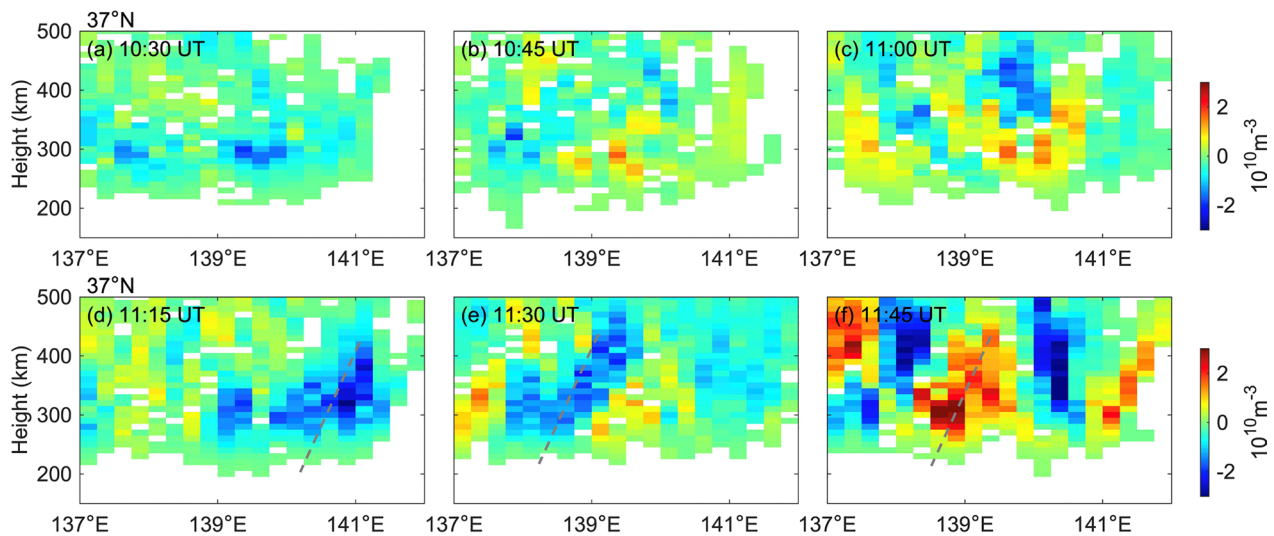
Fu *et al. Earth, Planets and Space* (2024) 76:102

Page 11 of 13



**Fig. 8** Vertical structures of reconstructed electron density perturbations at 37° N at different time epochs from 10:30 to 11:45 UT on July 4, 2022

Same as Fig. 7, Fig. 8 shows the vertical structures of reconstructed electron density perturbations in the zonal cross section for corresponding epochs. According to the 2-D maps, wavelike MSTID structures at 37° N occur after 11:00 UT. These perturbations are also reconstructed successfully in the vertical plane. In the zonal slice, the reconstruction results show a preferred alignment pattern, running from the high-east to the low-west. Furthermore, as shown in additional file 1: Figure S1, the southwestward propagation of nighttime MSTIDs at a speed of 100 m/s can be clearly observed in the NE-SW-vertical slice; these speeds are consistent with earlier analyses of nighttime MSTIDs using 2-D TEC perturbation maps (e.g., Matsushima et al., (2022)). Note that these reconstructions are performed using the GEONET and a portion of SoftBank receivers. The performance of the 3-D tomography technique depends on the density and spatial distribution of the signal ray paths within the volume of interest. Therefore, we anticipate that a denser network would enhance performance and fidelity, motivating future analyses to address even more complex ionospheric inhomogeneities.

## 5 Conclusions

This research developed a CIT technique capable of reconstructing the 3-D structures of electron density perturbations with high spatiotemporal resolution (0.25° in latitude and longitude, 10 km in altitude, 30 s in time). To facilitate the CIT, we utilized ultra-dense TEC measurements in Japan from two receiver networks provided by GEONET and SoftBank. In this tomography algorithm, TEC perturbations computed by subtracting a 30-min running average from

observations are combined with the background generated by IRI-2016 model to produce STECs for tomography, which enables imaging of disturbances with small amplitudes and scales. Validation from simulations demonstrated that the CIT technique could reconstruct the F-region perturbations with good fidelity; 80% of the original picture was reconstructed. The effectiveness of the algorithm is further exhibited when applied to a typical 3-D case study of nighttime MSTIDs on July 4, 2022.

For the first time, we have successfully reconstructed the field-aligned structures of nighttime MSTIDs with electrodynamic signatures at high spatiotemporal resolution. The MSTIDs initially form at lower altitudes (250–350 km), then develop to large amplitudes and scales, and extend to higher altitudes (300–500 km). Based on this developed CIT technique, we are now equipped to meticulously analyze the 3-D structural variations of ionospheric disturbances. Future research should concentrate on analyzing the characteristics of ionospheric disturbances originating from different sources (e.g., neutral and/or electrodynamic factors) in the vertical domain. This is important for a deeper understanding of the mechanisms underlying ionospheric disturbances at mid-latitudes.

## Abbreviations

| | |
|---|---|
| CIT | Computerized ionospheric tomography |
| Es | Sporadic E |
| GEONET | GNSS Earth Observation Network System |
| GNSS | Global navigation satellite systems |
| IED | Ionospheric electron density |
| IGRF | International Geomagnetic Reference Field |
| IPP | Ionospheric pierce points |
| LOS | Line of sight |

Fu *et al. Earth, Planets and Space*      (2024) 76:102

Page 12 of 13

| | |
|---|---|
| TEC | Total electron content |
| TECP | Total electron content perturbation |
| MSTID | Medium-scale traveling ionospheric disturbance |
| SLM | Single-layer model |
| STEC | Slant total electron content |
| VTEC | Vertical electron content |
| 2-D | Two-dimensional |
| 3-D | Three-dimensional |

## Supplementary Information

The online version contains supplementary material available at https://doi.org/10.1186/s40623-024-02051-2.

Additional file 1.

## Availability of data and materials
The GNSS observation data from GEONET can be accessed at the Geospatial Information Authority of Japan (GSI; https://www.gsi.go.jp/ ENGLISH/geonet_english.html). The SoftBank's GNSS observation data used in this study was provided by SoftBank Corp. and ALES Corp. through the framework of the "Consortium to utilize the SoftBank original reference sites for Earth and Space Science". The Dst data are provided by the World Data Center for Geomagnetism at http://wdc.kugi.kyoto-u.ac.jp/dstdir/index.html.

## Declarations

### Ethics approval and consent to participate
Not applicable.

### Consent for publication
Not applicable

### Competing interests
The authors declare that they have no competing interests.

### Author details
[1]Institute for Space-Earth Environmental Research, Nagoya University, Nagoya, Japan. [2]4DSpace, Department of Physics, University of Oslo, Oslo, Norway.

## References
Alken P, Thébault E, Beggan CD, Amit H, Aubert J, Baerenzung J, Zhou B (2021) International geomagnetic reference field: the thirteenth generation. Earth Planets Space 73(1):1–25. https://doi.org/10.1186/s40623-020-01288-x

Austen JR, Franke SJ, Liu C (1988) Ionospheric imaging using computerized tomography. Radio Sci 23(3):299–307. https://doi.org/10.1029/RS023i003p00299

Behnke R (1979) F layer height bands in the nocturnal ionosphere over Arecibo. J Geophys Res Space Phys 84(A3):974–978. https://doi.org/10.1029/JA084iA03p00974

Bilitza D, Altadill D, Truhlik V, Shubin V, Galkin I, Reinisch B, Huang X (2017) International Reference Ionosphere 2016: From ionospheric climate to real-time weather predictions. Space Weather 15(2):418–429. https://doi.org/10.1002/2016SW001593

Bowman G (1990) A review of some recent work on mid-latitude spread-F occurrence as detected by ionosondes. J Geomagn Geoelectr 42(2):109–138. https://doi.org/10.5636/jgg.42.109

Chen CH, Saito A, Lin CH, Yamamoto M, Suzuki S, Seemala GK (2016) Medium-scale traveling ionospheric disturbances by three-dimensional ionospheric GPS tomography. Earth Planets Space 68(1):1–9. https://doi.org/10.1186/s40623-016-0412-6

Cosgrove RB, Tsunoda RT (2004) Instability of the E-F coupled nighttime midlatitude ionosphere. J Geophys Res Space Phys. https://doi.org/10.1029/2003JA010243

Fu W, Ssessanga N, Yokoyama T, Yamamoto M (2021) High-resolution 3-D imaging of daytime sporadic-E over Japan by using GNSS TEC and ionosondes. Space Weather 19(12):e2021SW002878. https://doi.org/10.1029/2021SW002878

Fu W, Yokoyama T, Ssessanga N, Yamamoto M, Liu P (2022) On using a double-thin-shell approach and TEC perturbation component to sound nighttime mid-latitude E-F coupling. Earth Planets Space 74(1):1–17. https://doi.org/10.1186/s40623-022-01639-w

Fu W, Yokoyama T, Ssessanga N, Ma G, Yamamoto M (2023) Nighttime Midlatitude E-F Coupling in Geomagnetic Conjugate Ionospheres: A Double Thin Shell Model and a Multi-Source Data Investigation. J Geophys Res Space Phys 128(3):e2022JA031074. https://doi.org/10.1029/2022JA031074

Fu W, Otsuka Y, Shinbori A, Nishioka M, Perwitasari S (2024) Performance of the double-thin-shell approach for studying nighttime medium-scale traveling ionospheric disturbances using two dense GNSS observation networks in Japan. Earth Planets Space 76(1):7. https://doi.org/10.1186/s40623-023-01956-8

Haldoupis C (2012) Midlatitude sporadic E. A typical paradigm of atmosphere-ionosphere coupling. Space Sci Rev 168:441–461. https://doi.org/10.1007/s11214-011-9786-8

Hunsucker RD (1982) Atmospheric gravity waves generated in the high-latitude ionosphere: a review. Rev Geophys 20(2):293–315. https://doi.org/10.1029/RG020i002p00293

Jin S, Wang Q, Dardanelli G (2022) A review on multi-GNSS for earth observation and emerging applications. Remote Sens 14(16):3930. https://doi.org/10.3390/rs14163930

Kelley MC, Fukao S (1991) Turbulent upwelling of the mid-latitude ionosphere: 2. Theoretical framework. J Geophys Res Space Phys 96(A3):3747–3753. https://doi.org/10.1029/90JA02252

Kunitsyn VE, Tereshchenko ED (2003) Ionospheric tomography. Springer Sci Bus Media. https://doi.org/10.1007/978-3-662-05221-1

Lu W, Ma G, Wan Q (2021) A review of voxel-based computerized ionospheric tomography with GNSS ground receivers. Remote Sens 13(17):3432. https://doi.org/10.3390/rs13173432

Mannucci A, Wilson B, Yuan D, Ho C, Lindqwister U, Runge T (1998) A global mapping technique for GPS-derived ionospheric total electron content measurements. Radio Sci 33(3):565–582. https://doi.org/10.1029/97RS02707

Matsushima R, Hosokawa K, Sakai J, Otsuka Y, Ejiri MK, Nishioka M, Tsugawa T (2022) Propagation characteristics of sporadic E and medium-scale traveling ionospheric disturbances (MSTIDs): statistics using HF Doppler and GPS-TEC data in Japan. Earth Planets Space 74(1):60. https://doi.org/10.1186/s40623-022-01616-3

Otsuka Y, Kotake N, Shiokawa K, Ogawa T, Tsugawa T, Saito A. (2011) Statistical study of medium-scale traveling ionospheric disturbances observed with a GPS receiver network in Japan. In: Aeronomy of the Earth's Atmosphere and Ionosphere. Springer, Dordrecht. pp. 291–299. https://doi.org/10.1007/978-94-007-0326-1_21

Perkins F (1973) Spread F and ionospheric currents. J Geophys Res 78(1):218–226. https://doi.org/10.1029/JA078i001p00218

Saito A, Fukao S, Miyazaki S (1998) High resolution mapping of TEC perturbations with the GSI GPS network over Japan. Geophys Res Lett 25(16):3079–3082. https://doi.org/10.1029/98GL52361

Seker I, Livneh DJ, Makela JJ, Mathews JD (2008) Tracking F-region plasma depletion bands using GPS-TEC, incoherent scatter radar, and all-sky imaging at Arecibo. Earth Planets Space 60:633–646. https://doi.org/10.1186/BF03353127

Shiokawa K, Ihara C, Otsuka Y, Ogawa T (2003a) Statistical study of nighttime medium-scale traveling ionospheric disturbances using midlatitude airglow images. J Geophys Res Space. https://doi.org/10.1029/2002JA009491

Shiokawa K, Otsuka Y, Ihara C, Ogawa T, Rich FJ (2003b) Ground and satellite observations of nighttime medium-scale traveling ionospheric disturbance at midlatitude. J Geophys Res Space Phys. https://doi.org/10.1029/2002JA009639

Song R, Hattori K, Zhang X, Liu J-Y, Yoshino C (2021) Detecting the ionospheric disturbances in Japan using the three-dimensional computerized tomography. J Geophys Res Space Phys 126(6):e2020JA028561. https://doi.org/10.1029/2020JA028561

Ssessanga N, Kim YH, Kim E (2015) Vertical structure of medium-scale traveling ionospheric disturbances. Geophys Res Lett 42(21):91569165. https://doi.org/10.1002/2015GL066093

Ssessanga N, Kim YH, Jeong SH (2017) A statistical study on the F2 layer vertical variation during nighttime medium-scale traveling ionospheric disturbances. J Geophys Res Space Physics 122(3):3586–3601. https://doi.org/10.1002/2016JA023463

Tsugawa T, Kotake N, Otsuka Y, Saito A (2007) Medium-scale traveling ionospheric disturbances observed by GPS receiver network in Japan: a short review. GPS Solut 11:139–144. https://doi.org/10.1007/s10291-006-0045-5

Tsugawa T, Nishioka M, Ishii M, Hozumi K, Saito S, Shinbori A, Supnithi P (2018) Total electron content observations by dense regional and worldwide international networks of GNSS. J Disast Res 13(3):535–545. https://doi.org/10.20965/jdr.2018.p0535

Yamamoto M, Ono T, Oya H, Tsunoda RT, Larsen MF, Fukao S, Yamamoto M (1998) Structures in sporadic-E observed with an impedance probe during the SEEK campaign: comparisons with neutral-wind and radar-echo observations. Geophys Res Lett 25(11):1781–1784. https://doi.org/10.1029/98GL00709

Yang TY, Kwak YS, Kil H, Lee YS, Lee WK, Lee JJ (2015) Occurrence climatology of F region field-aligned irregularities in middle latitudes as observed by a 40.8 MHz coherent scatter radar in Daejeon, South Korea. J Geophys Res Space Phys 120(11):10107–10115. https://doi.org/10.1002/2015JA021885

Yokoyama T, Hysell DL, Otsuka Y, Yamamoto M (2009) Three-dimensional simulation of the coupled Perkins and Es-layer instabilities in the nighttime midlatitude ionosphere. J Geophys Res Space Phys. https://doi.org/10.1029/2008JA013789

## Publisher's Note